High Power Laser Science and Engineering, (2024), Vol. 12, e24, 11 pages.
doi:10.1017/hpl.2024.3

HIGH POWER LASER SCIENCE AND ENGINEERING

RESEARCH ARTICLE

The importance of Righi–Leduc heat flux to the ablative Rayleigh–Taylor instability during a laser irradiating targets

Ye Cui[1], Xiao-Hu Yang[1,5], Yan-Yun Ma[2,5], Guo-Bo Zhang[1], Bi-Hao Xu[1], Ze-Hao Chen[1], Ze Li[1], Fu-Qiu Shao[3], and Jie Zhang[4,5]

[1] *Department of Nuclear Science and Technology, National University of Defense Technology, Changsha, China*

[2] *College of Advanced Interdisciplinary Studies, National University of Defense Technology, Changsha, China*

[3] *Department of Physics, National University of Defense Technology, Changsha, China*

[4] *Key Laboratory for Laser Plasmas (Ministry of Education), School of Physics and Astronomy, Shanghai Jiao Tong University, Shanghai, China*

[5] *Collaborative Innovation Centre of IFSA, Shanghai Jiao Tong University, Shanghai, China*

(Received 8 September 2023; revised 7 December 2023; accepted 16 January 2024)

Abstract

The Righi–Leduc heat flux generated by the self-generated magnetic field in the ablative Rayleigh–Taylor instability driven by a laser irradiating thin targets is studied through two-dimensional extended-magnetohydrodynamic simulations. The perturbation structure gets into a low magnetization state though the peak strength of the self-generated magnetic field could reach hundreds of teslas. The Righi–Leduc effect plays an essential impact both in the linear and nonlinear stages, and it deflects the total heat flux towards the spike base. Compared to the case without the self-generated magnetic field included, less heat flux is concentrated at the spike tip, finally mitigating the ablative stabilization and leading to an increase in the velocity of the spike tip. It is shown that the linear growth rate is increased by about 10% and the amplitude during the nonlinear stage is increased by even more than 10% due to the feedback of the magnetic field, respectively. Our results reveal the importance of Righi–Leduc heat flux to the growth of the instability and promote deep understanding of the instability evolution together with the self-generated magnetic field, especially during the acceleration stage in inertial confinement fusion.

Keywords: amplitude; linear growth rate; Rayleigh–Taylor instability; Righi–Leduc heat flux; self-generated magnetic field

1. Introduction

The Rayleigh–Taylor instability (RTI) is ubiquitous in high energy density physics, such as laboratory astrophysics experiments and inertial confinement fusion (ICF)[1–3]. The RTI occurs when a light fluid supports a heavy fluid in external gravity field, which features the growth of perturbation amplitude on the interface between two fluids[4,5]. In laser fusion experiments, the perturbation seeded by target defect or drive asymmetry could be significantly amplified by the RTI[6]. Due to the energy transfer creating a continuous density profile on the interface, the linear growth is stabilized compared to the classical case and a cutoff wavelength appears when the perturbation wavelength is sufficiently short[7]. Therefore, the ablative RTI (ARTI) is commonly called to emphasize the importance of the mass ablation[8,9]. The ARTI mainly occurs at the ablation front separating the compressed target from the blow-off corona plasma and the inner interface between the fuel shell and the hot spot[10,11]. This instability could destroy the shell integrity and limit the implosion efficiency during the acceleration stage. What is worse, it would aggravate the material mixing, reduce the effective size of the hot spot and even result in ignition failure[12]. Control of the ARTI at an acceptable level is crucial to improve fusion performance.

Correspondence to: Xiao-Hu Yang and Guo-Bo Zhang, Department of Nuclear Science and Technology, National University of Defense Technology, Changsha 410073, China. Email: xhyang@nudt.edu.cn; zgb830@163.com; Yan-Yun Ma, College of Advanced Interdisciplinary Studies, National University of Defense Technology, Changsha 410073, China. Email: yanyunma@126.com

As an inevitable process in ICF and the general laser–plasma interaction, the intense magnetic field could be spontaneously self-generated by a number of mechanisms, including but not limited to the thermoelectric effect and anisotropic velocity distribution of hot electrons, with relative importance depending on the interaction parameters[13–15]. For the interaction with solid targets of nanosecond lasers, the Biermann battery effect is regarded as the primary source, caused by nonparallel gradients between temperature and density[16,17]. The mechanism behind magnetic field generation is the loss of electron energy, resulting in the breakdown of local neutrality. In recent years, the self-generated magnetic field has been studied analytically, experimentally and numerically by many researchers. Li *et al.*[18] utilized the monoenergetic proton radiography method to measure the electromagnetic field generated during the interaction of a solid target and long-pulse laser beams. Due to the fact that the target surface cannot be perfectly smooth, the perturbation-induced magnetic field attracts great attention. As early as the 1970s, Mima *et al.*[19] demonstrated the presence of the magnetic field in a plasma subject to the RTI from the perspectives of theory and simulation. The first experimental demonstration was published in 2012, which reported the generation of a several-tesla magnetic field during the linear stage and motivated further investigation of RTI-induced magnetic fields[20,21]. The magnetic field strength could reach up to the megagauss level during the nonlinear growth phase in an ablatively driven plasma[22]. The self-generated magnetic field could play a stabilizing or destabilizing role depending on the Froude number during the linear stage[23]. Zhang *et al.*[24] also found that the Nernst compressed magnetic field reduced the bubble width and boosted the bubble velocity during the nonlinear stage in ARTI relevant to ICF implosion. During the deceleration stage of ICF implosion, the self-generated magnetic field is as intense as thousands of teslas with a large Hall parameter and anisotropic heat flux would promote spike penetration[25]. During the stagnation phase, the magnetic field, initially appearing on the inner interface of the cold shell, could be pushed into the hot spot by the low-mode perturbation and degrade the fusion energy[26].

When a long-pulse laser irradiates targets, the pressure perturbation is generated by the laser imprint and further enhanced by the self-generated magnetic field due to a combination of the Nernst advection and the Righi–Leduc (R-L) heat flux[27]. This mechanism occurs in the early stage and the enhanced perturbation could be regarded as a seed perturbation for the hydrodynamic instability. The self-generated magnetic field indirectly feeds back on the hydrodynamic process through electron magnetization rather than the magnetic pressure[28]. Walsh *et al.*[25,26] demonstrated that the magnetized heat flux is highly significant both in the deceleration and stagnation stages of ICF. However, the importance in the acceleration stage still remains unknown. In this paper, we analyze the importance of the R-L heat flux to the ARTI in a laser irradiating thin targets based on the fully extended magnetohydrodynamic simulations. The rest of this paper is structured as follows. Section 2 briefly outlines the numerical code and the extended-magnetohydrodynamic model used for the results presented here. In Section 3, the ARTI evolution with a self-generated magnetic field included is studied. The simulations show that an increase in the linear growth rate and the amplitude is mainly attributed to the R-L effect deflecting the total heat flux. The less heat flux concentrated at the spike tip effectively lowers ablative stabilization and promotes instability growth. The importance of the nonlocal effect is discussed theoretically in Section 4. Finally, Section 5 gives the conclusion to the whole paper.

2. The simulation model

In this paper, numerical simulations are performed by using the open-source code FLASH[29]. FLASH is a highly parallel and multi-dimensional finite-volume Eulerian code, which solves the single-fluid governing equations and advances hydrodynamic evolution based on a directionally unsplit staggered mesh solver[30,31]. The code has been extended to three temperature treatments and is coupled with a variety of physical processes to improve the capability of simulating high energy density physics. Without considering external gravity, viscous force and radiation transport, the governing equations are described by the following equations:

$$\begin{aligned}
&\frac{\partial \rho}{\partial t} + \nabla \cdot \left(\rho \vec{v}\right) = 0, \\
&\frac{\partial}{\partial t}\left(\rho \vec{v}\right) + \nabla \cdot \left(\rho \vec{v}\,\vec{v} - \frac{\vec{B}\,\vec{B}}{4\pi}\right) + \nabla P_{\mathrm{tot}} = 0, \\
&\frac{\partial}{\partial t}\left(\rho E_{\mathrm{tot}}\right) + \nabla \cdot \left[\left(\rho E_{\mathrm{tot}} + P_{\mathrm{tot}}\right)\vec{v} - \frac{1}{4\pi}\vec{B}\left(\vec{B}\cdot\vec{v}\right)\right] \\
&\quad = Q_{\mathrm{L}} + Q_{\mathrm{res}} - \nabla \cdot \vec{q}\,,
\end{aligned} \tag{1}$$

where ρ, $\vec{v}$ and $\vec{B}$ are the density, velocity and magnetic field, respectively; $P_{\mathrm{tot}} = P_{\mathrm{ele}} + P_{\mathrm{ion}} + P_{\mathrm{mag}}$ is the total pressure defined as the sum over the electron pressure, ion pressure and magnetic pressure; $E_{\mathrm{tot}} = E_{\mathrm{int}} + E_{\mathrm{kin}} + E_{\mathrm{mag}}$ is the specific total energy defined as the sum over the internal energy, kinetic energy and magnetic energy. As for the heat flux $\vec{q}$, only the electron component is considered. Here, Q_{L} represents the laser energy deposition. The laser is treated as individual rays and the energy deposition is computed by using ray-tracing in the geometric optics approximation and inverse Bremsstrahlung. Further, Q_{res} is additional resistive heating caused by the magnetic fields and would be equivalent to the Ohmic heating $Q_{\mathrm{ohm}} = \eta j^2$ if there is no resistivity gradient, where j is the magnitude of the current density. In electrically conducting plasma, the magnetic field evolution can be described by the Faraday equation combined with the generalized Ohm's law:

https://doi.org/10.1017/hpl.2024.3 Published online by Cambridge University Press

$$\frac{\partial \vec{B}}{\partial t} = \nabla \times \left(\vec{v} \times \vec{B} \right) - \nabla \times \left(\frac{\vec{j} \times \vec{B}}{en_e} \right) - c\nabla \times \left(\frac{\overline{\overline{\alpha}} \cdot \vec{j}}{e^2 n_e^2} \right) + c\nabla \times \left(\frac{\overline{\overline{\beta}} \cdot \nabla T_e}{en_e} \right) + \frac{c}{e} \nabla \times \left(\frac{\nabla P_e}{n_e} \right), \quad (2)$$

where n_e is the electron number density, c is the speed of light in vacuum, e is the elementary charge and P_e is the electron thermal pressure[28,32]. The units are cgs, apart from the electron temperature T_e in eV. The third and fourth terms on the right-hand side of Equation (2) result from the friction force and the thermal force, respectively. The $\overline{\overline{\alpha}}$ and $\overline{\overline{\beta}}$ are the transport coefficient tensors according to Braginskii transport theory and are numerically corrected by Davies *et al.*[32,33]. Without any initial magnetic field, the seed magnetic field is generated due to the misaligned gradients of electron number density and thermal pressure, called the Biermann battery effect[20,22]. FLASH handles the Biermann battery term as an external magnetic field source via passive production of hydrodynamic variables. After solving the hydrodynamic equations, the thermal conduction is treated additionally and solved implicitly to relax the strict time step.

3. Two-dimensional simulations of the ablative Rayleigh–Taylor instability with the magnetic field included

As the RTI occurs on the ablation front in the acceleration stage, we firstly carry out two-dimensional (2D) simulations of a laser irradiating a thin target without perturbation to obtain the hydrodynamic behavior of the ablation front. The simulation domain is based on the x–y Cartesian coordinate. Periodic and outflow boundary conditions are imposed on the x- and y-directions, respectively. A schematic diagram is depicted in Figure 1. The target material is CH with an initial density of $\rho = 1.1$ g/cm^3 and a finite thickness of $d = 60$ μm. The upper surface is located at $y = 0$ and extended to $y = -60$ μm down the y-axis. A laser beam, operated at a wavelength of 0.35 μm, is incident from the upper boundary to the target surface. The laser has a square temporal profile with an intensity of $I = 6 \times 10^{14}$ W/cm^2 and a 0.1 ns linear rising ramp. The adaptive refinement grid method is applied with the minimum grid size of $\Delta x \times \Delta y = 0.25$ μm $\times$ 0.25 μm. Convergence tests are carried out and there is no significant difference in the magnitude of the self-generated magnetic field and the perturbation amplitude between the gird size of $\Delta = 0.25$ μm and that of $\Delta = 0.2$ μm. It is reasonably believed that $\Delta = 0.25$ μm can satisfy the stability condition for the current simulations here. The equation of state (EOS) in tabular form is calculated by the FEOS code[34].

When a laser beam is switched on, the energy deposition leads to the ablated material coming off the outer surface

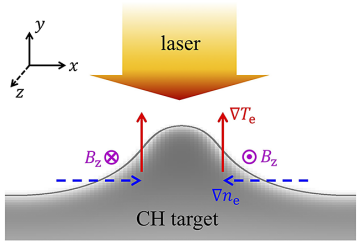

Figure 1. Schematic diagram of a laser driven RTI with the self-generated magnetic field included.

of the target and generates blow-off corona plasma. The shock driven by the ablation pressure propagates towards the target inside, and the material behind the shock front is compressed into higher density. Figure 2(a) shows the density distributions along the y-axis at different times. At $t = 0.2$ ns, the shock front locates at $y = -13.5$ μm and the peak density increases up to $\rho = 3.3$ g/cm^3. The shock front arrives at the rear of the target at $t = 0.8$ ns and the thickness is compressed to $d \sim 11$ μm with a peak density of $\rho = 4.4$ g/cm^3. Then the rarefaction wave is reflected towards the right and unloads the compressed target. At $t = 1.0$ ns, the peak density has decreased to $\rho = 2.7$ g/cm^3. Figure 2(b) shows that the velocity and the position of the ablation front evolve over time in the laboratory coordinate system. The velocity of the ablation front is equal to the sum over the ablation velocity penetrating into the target and the velocity of the shocked material. It can be seen that the ablation front moves at a constant velocity of 68 μm/ns before $t = 0.8$ ns. If there is initial perturbation modulation on the target surface, the ablation front would be firstly unstable to the Richtmyer–Meshkov instability (RMI) rather than the RTI due to the absence of acceleration[35]. When the reflected rarefaction wave arrives at the ablation front, the ablation front begins to be accelerated at $t = 0.85$ ns.

In the configuration of a laser irradiating a planar target, it was experimentally found that the magnetic field was concentrated on a hemispherical shell surrounding the ablative plasma bubble with the maximum amplitude appearing near the edge and falling to zero at the center[18]. The magnetic field has a toroidal configuration with scale length comparable to the spot size. If a perturbation occurs in the laser-irradiation region, the Biermann battery effect would be significantly enhanced and the RTI-induced magnetic field could reach higher strength. This mechanism can be seen in Figure 1.

In the follow-up paper, the 2D simulations upon introducing perturbation are further carried out and the self-generated magnetic field is simultaneously taken into account. Velocity perturbation taking the form of $\tilde{v}_y = v_0 \cos(kx) \exp(k|y - y_0|)$ is introduced as the initial instability seed at a moderate time, where $v_0 = 1$ μm/ns is the velocity perturbation amplitude, y_0 is the position of the ablation front, $k = 2\pi/\lambda$ and $\lambda = 20$ μm is the perturbation

https://doi.org/10.1017/hpl.2024.3 Published online by Cambridge University Press

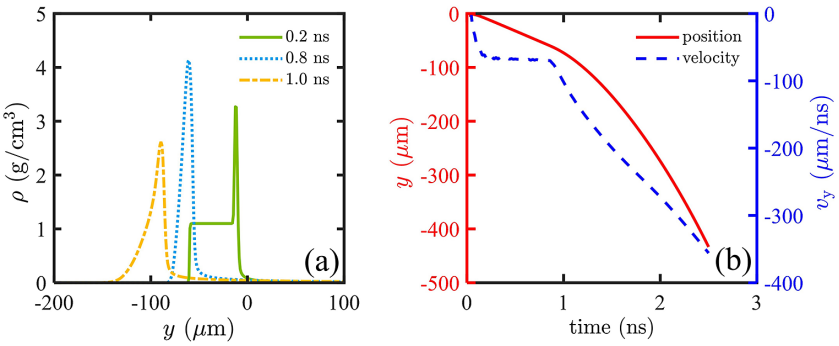

Figure 2. (a) The density distribution along the y-axis at different times. (b) The position (red-solid line) and velocity (blue-dashed line) of the ablation front evolve over time.

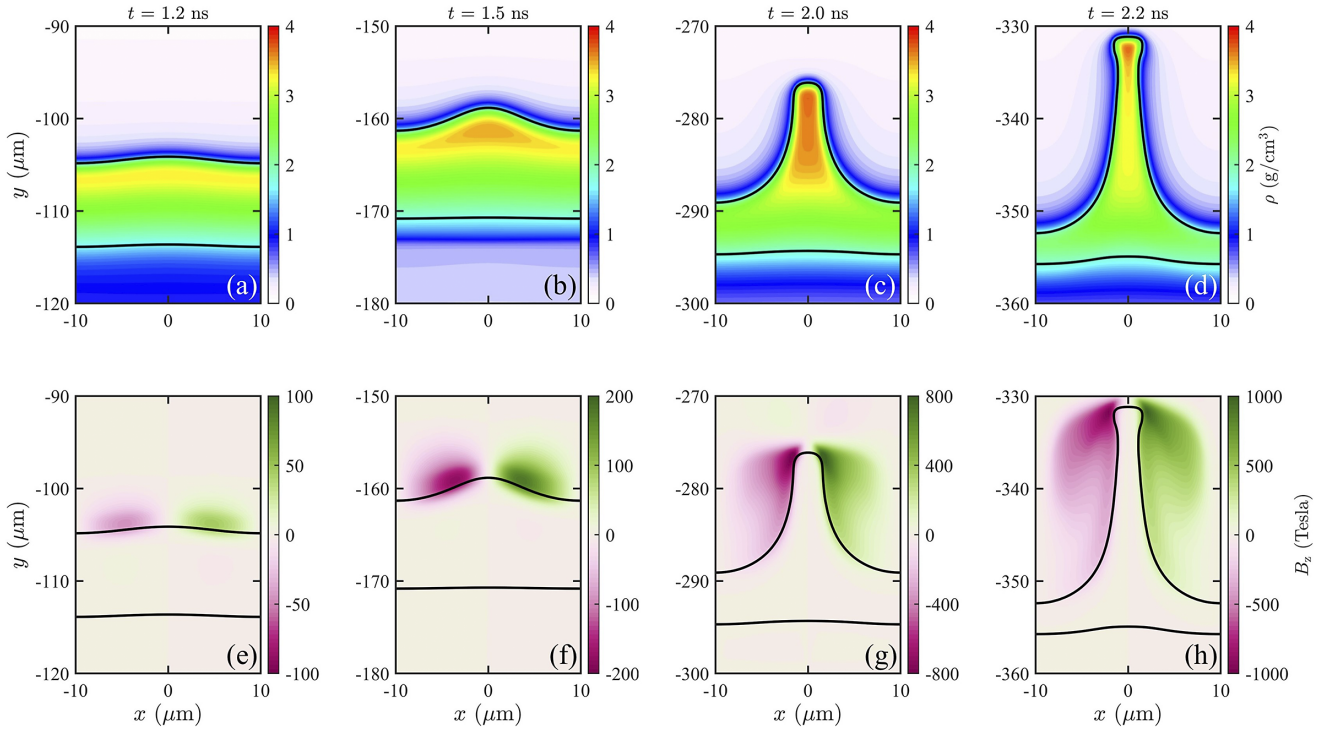

Figure 3. The spatial distributions of the density (a)–(d) and the magnetic field (e)–(h) at different times during the evolution of the RTI.

wavelength. The perturbation time of $t = 0.85$ ns is chosen as the moment when the deflected rarefaction wave arrives at the ablation front and the ablation front begins to accelerate.

The perturbation amplitude firstly grows exponentially in time. After a short linear stage, the RTI grows into the nonlinear regime and a bubble-spike structure is formed[36]. When the bubble-spike amplitude is comparable to its perturbation wavelength, the RTI evolves into the highly nonlinear regime. Figure 3 shows the spatial distributions of the density and magnetic field at different times. Since the interface between the cold-dense target and corona plasma is not sharp, we define the position with the minimum density scale length as the ablation front, which is shown by the black-solid line in Figure 3 and the follow-up figures, so that the instability amplitude could be easily tracked in numerical simulations. At the early time, the peak-to-valley (P-V) amplitude η continues to increase until linear saturation. In the following paper, 'P-V' is omitted for brevity. The magnetic field is generated near the ablation front. At $t = 1.20$ ns, the amplitude is $\eta_B = 0.70$ μm with peak field strength of 46 T. Then the magnetic field accumulates steadily and increases up to 179 T at $t = 1.50$ ns. The RTI grows into the nonlinear regime from $t = 1.63$ ns and the spike-bubble structure is formed. A jet-like spike rises up into the conduction region and the bubble penetrates into the target. It can be seen that the spike is wrapped around the magnetic field. The region with the maximum field strength is near the spike tip. The field strength continues to increase as the amplitude increases, reaching 825 T at $t = 2.0$ ns and 981 T at $t = 2.2$ ns.

The amplitude evolution is considered as an important measurement of the growth of the RTI, as shown in Figure 4.

https://doi.org/10.1017/hpl.2024.3 Published online by Cambridge University Press

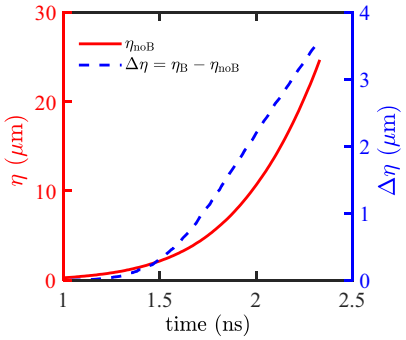

Figure 4. The peak-to-valley amplitude evolves over time without a magnetic field (red-solid line). The blue-dashed line is the amplitude difference between the amplitude with and without the magnetic field included.

It is usually thought that linear saturation occurs when the classical amplitude reaches $\eta_c \sim 0.1\lambda$, corresponding to the P-V amplitude (twice the classical amplitude) of $\eta = 4$ μm for the perturbation wavelength of $\lambda = 20$ μm. Linear saturation occurs at $t = 1.68$ ns without a magnetic field and $t = 1.63$ ns with a magnetic field considered, indicating that the magnetic field advances the moment of reaching linear saturation. The linear growth rate can be approximately derived as $\gamma = \ln\left(\frac{\eta_2}{\eta_1}\right)/(t_2 - t_1)$, where t_1 is chosen as the moment of $\eta \sim 0.02\lambda$ and t_2 is chosen as the moment of $\eta \sim 0.18\lambda$, spanning the range from 10% to 90% of the linear saturation. Here, η_1 and η_2 are the amplitudes at the moments of t_1 and t_2, respectively. The linear growth rates are exponentially fitted to be $\gamma_{noB} = 3.70\ \mathrm{ns}^{-1}$ without a magnetic field and $\gamma_B = 4.11\ \mathrm{ns}^{-1}$ with a magnetic field considered. The self-generated magnetic field leads to an increase in the linear growth by a factor of 11%. In the nonlinear stage, the amplitude is $\eta_{noB} = 10.66$ μm at $t = 2.0$ ns. The magnetic field also results in an increase by 21% and the amplitude reaches $\eta_B = 12.86$ μm at the same moment. In our simulations, the magnetic pressure is typically smaller than the thermal pressure, since $\beta \gg 1$, where β is the ratio of the thermal pressure to the magnetic pressure. The hydrodynamic evolution of the plasma is not directly affected by the presence of the magnetic field. The magnetic field can modify the plasma evolution indirectly by altering the thermal transport. We also carry out simulations with isotropic electron thermal conduction, that is, not considering the electron magnetization. The simulations show that the amplitude evolution is almost identical to the case without the self-generated magnetic field (not shown for brevity), indicating that an increase in growth rate and amplitude mainly contributes to the feedback of the magnetic field to the heat flux.

The Hall parameter χ_e is an important index of quantifying the plasma magnetization, which is a dimensionless parameter defined as the product of electron cyclotron frequency ω_{ce} and electron–ion collision time τ_{ei}. The Hall parameter depends on the magnetic field strength, electron temperature and electron number density. In a magnetized plasma, the presence of the magnetic field modifies the thermal conduction coefficients and the heat flux is regarded as anisotropic[32]. The magnetized electron thermal conduction can be expressed as follows:

$$\vec{q}_e = -\kappa_\parallel \nabla_\parallel T_e - \kappa_\perp \nabla_\perp T_e - \kappa_\wedge \left(\vec{b} \times \nabla T_e\right), \qquad (3)$$

where $\vec{b}$ is the unit vector along the magnetic field lines. $\kappa_\parallel$ is the thermal coefficient along the magnetic field line and is numerically equal to the coefficient in the absence of a magnetic field and $\kappa_\perp$ is the thermal coefficient perpendicular to the magnetic field. Due to the magnetic field inhibiting the heat carrying electrons, $\kappa_\perp$ decreases as the Hall parameter increases, leading to a flux limiter of heat flux that is perpendicular to magnetic field. The $\kappa_\wedge$ term is additionally generated due to the electron deflection and is perpendicular to both the temperature gradient and magnetic field lines, and is known as the R-L effect. As the Hall parameter increases, $\kappa_\wedge$ firstly increases until reaching a peak value and then decreases monotonically. The $\kappa_\perp$ and $\kappa_\wedge$ coefficients, called perpendicular and cross-thermal coefficients in the following paper, depend on the Hall parameter and effective ionization. If a plasma is unmagnetized, only the first two terms on the right-hand side of Equation (3) are retained. Here, $\kappa_\perp$ is equal to $\kappa_\parallel$, resulting in anisotropic heat flux degenerating into the isotropic description. In this paper, the thermal coefficients improved by Ji and Held[37] are employed.

Figure 5(a) shows the spatial distribution of Hall parameters at $t = 2.0$ ns, and the RTI evolution is in the nonlinear regime. The plasma near the spike tip is magnetized and the peak value of the Hall parameter is $\chi_e \sim 0.15$. Although the plasma is still in a low magnetization state, the anisotropic thermal condition caused by the magnetic field is of high importance. As for the cross-component, $\kappa_\wedge/\kappa_\parallel$ reaches approximately 0.1 at $\chi_e \sim 0.02$, meaning that the R-L heat flux cannot be negligible. Figures 5(b) and 5(c) show the ratio of the perpendicular and cross-components to the parallel thermal coefficients $\kappa_\perp/\kappa_\parallel$ and $\kappa_\wedge/\kappa_\parallel$ at the same moment. The $\kappa_\perp$ coefficient decreases to 84% and the $\kappa_\wedge$ coefficient generated additionally reaches 41% of the parallel thermal coefficient $\kappa_\parallel$. The spatial distribution of the self-generated magnetic field is like a cover that wraps around the spike tip and suppresses the ablation from the hot conduction region.

Figure 6(a) displays the total heat flux with a magnetic field (pink-dashed-dot line), which is superimposed on the density distribution at $t = 2.0$ ns. The streamline without a magnetic field (yellow-solid line) is meanwhile shown as a comparison. The critical density surface is chosen as the starting points of the heat flux streamlines, since laser energy deposition occurs near the critical density surface and the conduction region is dominated by electron thermal conduction. As the magnetic field is generated azimuthally

https://doi.org/10.1017/hpl.2024.3 Published online by Cambridge University Press

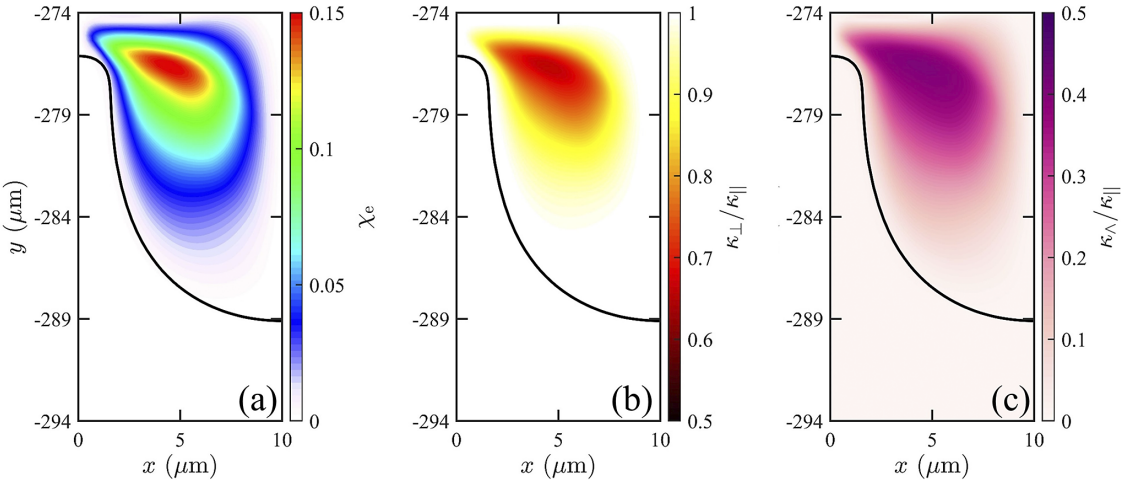

Figure 5. Spatial distributions of (a) the Hall parameter χ_e, (b) the ratio of perpendicular to parallel thermal transport coefficients $\kappa_\perp/\kappa_\parallel$ and (c) the ratio of cross to parallel thermal transport coefficients $\kappa_\wedge/\kappa_\parallel$ at $t = 2.0$ ns. Only the right-hand side of the spike is shown.

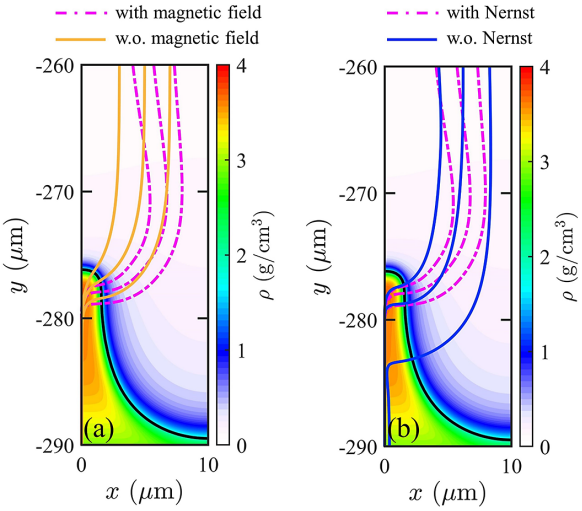

Figure 6. At $t = 2.0$ ns, a comparison of heat flux streamlines with (without) a magnetic field (a), and with (without) the Nernst effect (b) overlaid on the density spatial distribution. Only the right-hand side of the spike is shown. The pink-dashed-dot lines in (a) and (b) are identical.

along the z-axis and without x- and y-components in 2D simulations, there is no component of the heat flow along the magnetic field lines. In the region above $y = -250$ μm, the Hall parameter is only $\chi_e \sim 0.02$ with a several-tesla magnetic field. The two streamlines of the heat flux almost overlap, as the magnetic field has almost no effect on heat flux. Compared to the case without a magnetic field, the magnetized heat flux is deflected to the right when flowing into the region below $y = -255$ μm. The R-L effect deflects the heat flow along the spike and towards the base, and diverts the heat flux near the spike tip. Without a magnetic field included, the heat flow is concentrated at the spike tip, enhancing the spike ablation. The R-L term cools the spike tip, lowers the ablative stabilization, allows the perturbation to penetrate further into the conduction region and naturally increases the amplitude.

Although the magnetization is still at a low level with $\chi_e \leq 0.15$, as the spike-bubble structure is cold in temperature and high in density, the simulations show that the R-L effect has a non-ignorable influence. In order to further analyze the importance of the R-L heat flux, we artificially multiply the original $\kappa_\wedge$ by a factor $f_\wedge$ and fix the other thermal conduction coefficients. Figure 7(a) shows the velocity of the spike tip and the bubble vertex at $t = 2.0$ ns for different $f_\wedge$. The velocity is diagnosed in the reference frame of the ablation front. As $f_\wedge$ increases, the R-L effect deflects more and more heat flux away from the spike tip and inhibits the spike ablation. The spike velocity increases from 26.46 μm/ns with $f_\wedge = 0.2$ to 31.08 μm/ns with $f_\wedge = 1.2$, meaning that the spike penetrates into the conduction region deeply. There is no significant change in the bubble velocity, as the transport of the magnetic field into the bubble is suppressed by the Nernst effect. The thermal transport inside the bubble is prone to be isotropic. The faster spike velocity results in an increase in the linear growth rate and the nonlinear amplitude, which are shown in Figure 7(b). When the R-L effect is switched off, corresponding to the case of $f_\wedge = 0$, the linear growth rate and the amplitude are $\gamma = 3.73$ ns^{-1} and $\eta = 10.80$ μm, respectively, only a little higher than the case without magnetic field $(\gamma = 3.70\ \text{ns}^{-1}, \eta = 10.66\ \mu\text{m})$, because the perpendicular thermal coefficient $\kappa_\perp$ also has the potential to suppress the spike ablation. The slight increase reveals that the contribution of the R-L heat flux is more important than that of the perpendicular heat flux, especially for the case with a small Hall parameter. The linear growth rate increases up to $\gamma = 4.16$ ns^{-1} for the $f_\wedge = 1.2$ case. This method demonstrates the importance of the R-L effect to the evolution of the RTI, although it is a little physically unreasonable.

In order to understand comprehensively the influence of the magnetic field on RTI growth, the thermal driven terms in Equation (2) are re-arranged into a form that is similar to

https://doi.org/10.1017/hpl.2024.3 Published online by Cambridge University Press

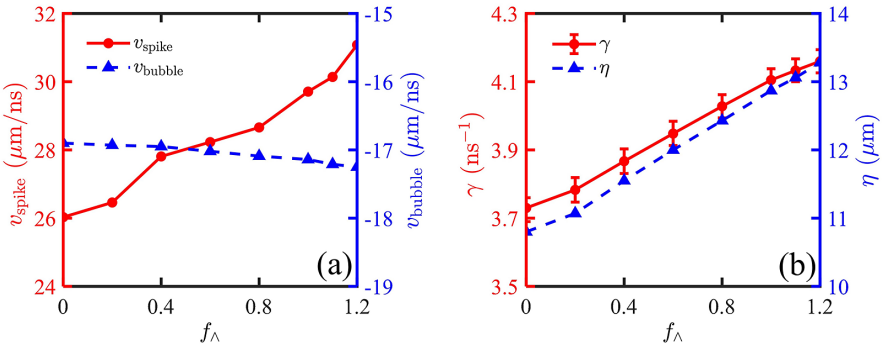

Figure 7. At $t = 2.0$ ns, (a) the velocity of the spike tip (red-circle line) and the bubble vertex (blue-delta line), and (b) the linear growth rate (red-circle line) and the amplitude (blue-delta line) for different $f_\wedge$ factors.

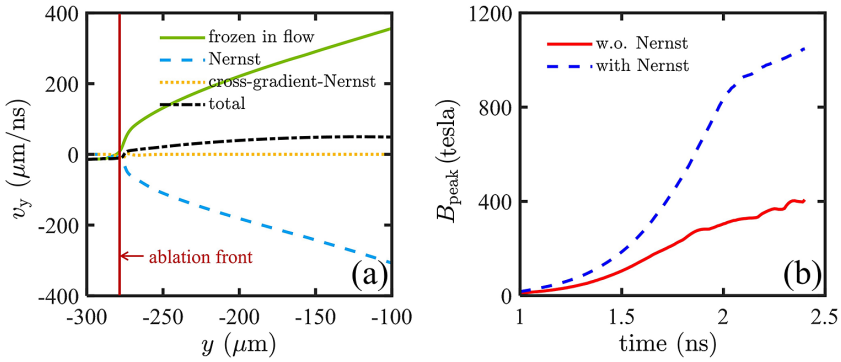

Figure 8. (a) Distributions of the y-component of the fluid velocity (green-solid line), the Nernst advection velocity (blue-dashed line) and the cross-gradient Nernst velocity (yellow-dot line) and the total velocity (black-dashed-dot line), which are diagnosed at the right-hand side of the spike $x = 5.0$ μm at $t = 2.0$ ns. (b) The peak magnitudes of the magnetic field evolve over time without (red-solid line) and with (blue-dashed line) the Nernst effect.

the advection velocity. The transport of the magnetic field can be written in a physically motivated form as follows:

$$\frac{\partial \vec{B}}{\partial t} = \nabla \times \left(\vec{v}_{\text{eff}} \times \vec{B} \right) - \nabla \times \frac{c^2 \eta}{4\pi} \left(\nabla \times \vec{B} \right) + \frac{c}{e} \nabla \times \left(\frac{\nabla P_e}{n_e} \right), \tag{4}$$

$$\vec{v}_{\text{eff}} = \vec{v} - \frac{c\beta_\wedge}{e n_e \mid \vec{B} \mid} \nabla T_e - \frac{c\left(\beta_\parallel - \beta_\perp\right)}{e n_e \mid \vec{B} \mid} \left(\vec{b} \times \nabla T_e \right). \tag{5}$$

The terms on the right-hand side of Equation (4) are the effective advection, diffusion with the resistivity of η and the Biermann battery effect, respectively[38]. As expressed in Equation (5), the effective advection velocity $\vec{v}_{\text{eff}}$ is defined as the sum of the fluid velocity, Nernst velocity and cross-gradient Nernst velocity. The magnetic Reynolds number Re_m is used to evaluate the relative importance between the frozen-in-flow and resistive diffusion. In the conduction region, $\text{Re}_m = \frac{lv}{D_m}$ is calculated to be approximately 10 or even greater, where the wavelength of $\lambda = 20$ μm is chosen as the characteristic scale length, the average blow-out velocity $v = 200$ μm/ns is regarded as the fluid characteristic velocity and $D_m = \frac{c^2\eta}{4\pi} \sim 4.1 \times 10^3$ cm^2/s is the magnetic diffusion coefficient, indicating that the magnetic diffusion is negligible reasonably. The transport of the magnetic field is mainly dominated by the frozen-in-flow and thermally driven terms, with the latter resulting in the Nernst and cross-gradient Nernst advection, and the convection of the magnetic field is further retreated as $\frac{\partial \vec{B}}{\partial t} = \nabla \times \left(\vec{v}_{\text{eff}} \times \vec{B} \right) + \frac{c}{e} \nabla \times \left(\frac{\nabla P_e}{n_e} \right)$.

Magnetic field advection is a balance between the frozen-in-flow with ions and the thermally driven effects, and the latter provides an additionally convective velocity along the heat flux[39,40]. The Nernst effect convects the magnetic field down the temperature gradient and the cross-gradient Nernst tends to advect the magnetic field towards the spike base. The Nernst flux limiter is equal to the thermal flux limiter and is chosen to be $f = 0.1$ here. The Nernst flux limiter is used to limit the Nernst velocity. Figure 8(a) displays the y-component of the plasma velocity as well as thermally driven velocity at $t = 2.0$ ns. The former is obtained in the reference frame of the ablation front, just like the velocity of the spike tip and the bubble vertex in Figure 7(a). The total velocity is also plotted in Figure 8(a). It is observable that the Nernst velocity assumes the opposite direction but maintains the same magnitude as the fluid velocity with a few hundreds of μm/ns. The cross-gradient Nernst velocity

https://doi.org/10.1017/hpl.2024.3 Published online by Cambridge University Press

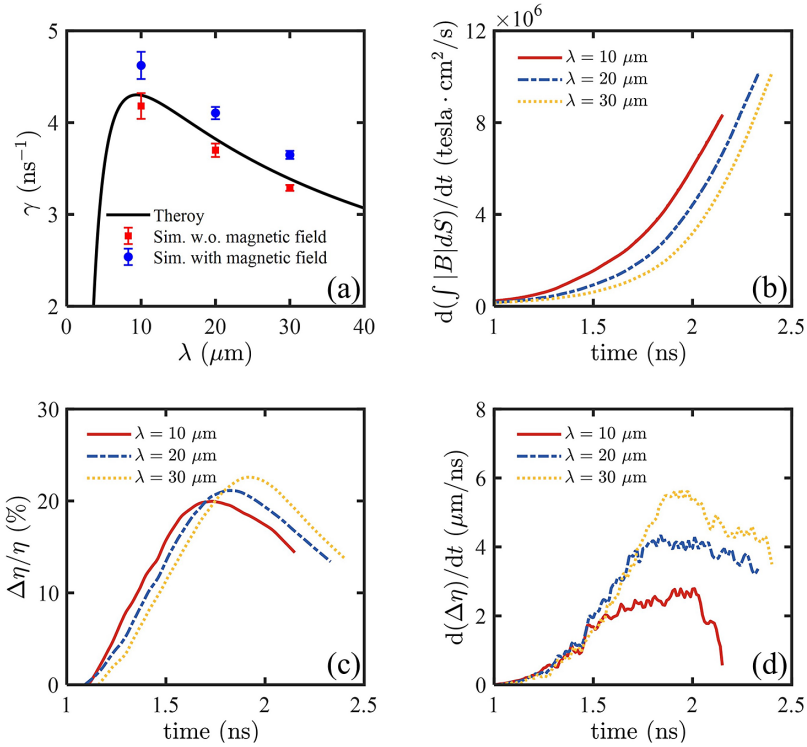

Figure 9. (a) Comparison of the linear growth rate. The black-solid line is the theoretical prediction. The red circles are from the simulations without a magnetic field, while the blue squares correspond to cases with a magnetic field included. The generation rate of the self-generated magnetic field (b), the percentage increase (c) and the derivative of the amplitude difference (d) evolve over time for different wavelengths.

is much smaller than the Nernst velocity due to low magnetization and small temperature gradient along the x-axis. The total advection velocity is closer to zero, meaning that the self-generated magnetic field rapidly accumulates locally. This phenomenon is beneficial for an increase in the field strength. Figure 8(b) shows a comparison of the evolution of the peak magnitude of the magnetic field over time. When the Nernst effect is included, the magnetic field is compressed and amplified near the ablation front. At $t = 2.0$ ns, the peak strength almost reaches 800 T, nearly three times higher than the case without the Nernst effect. In addition, the magnetic field exhibits wider spatial distribution in the absence of the Nernst advection. Compared to the case with the Nernst effect, the R-L term deflects the heat flux in the region farther away from the ablation front, which is shown in Figure 6(b). The simulation shows that the linear growth rate without the Nernst effect is about $\gamma = 4.18$ ns^{-1} and the amplitude at $t = 2.0$ ns is $\eta = 13.72$ μm, both higher than the case with the Nernst effect included, indicating that the Nernst effect is beneficial to smoothing the instability growth.

Figure 9(a) shows a comparison between the linear growth rates without and with the self-generated magnetic field for different wavelengths. In order to theoretically predict the linear growth rate, the laser irradiating the planar target without perturbation is simulated to get the distribution of density and pressure near the ablation front. Then the fitting method in Ref. [41] is employed to obtain variables including the density scale length L_0, Froude number Fr, acceleration g and ablation velocity v_a, averaged between $t_1 = 1.09$ and $t_2 = 1.59$ ns, which are shown in Table 1. The selected time window corresponds to the linear stage for $\lambda = 20$ μm. Then these averaged variables are substituted into Equation (8) in Ref. [41] to get the theoretical growth rates for different wavelengths, which are shown by the black-solid line. Without the self-generated magnetic field, the growth rate agrees well with the theoretical prediction. The magnetic field increases the growth rate by approximately 10%. As for high perturbation with the shorter wavelength, the perturbation could be increased by even more than 10%. It is shown that the self-generated magnetic field plays a destabilizing role for the cases with a small Froude number and our simulation agrees qualitatively with Ref. [23].

Table 1. The averaged values used to theoretically predict the linear growth rate for different wavelengths.

L_0 (μm)	Fr	g (μm/ns^2)	v_a (μm/ns)
0.25	0.31	162.60	3.54

Figure 9(c) shows the percentage increase in perturbation amplitude during the whole process for three wavelengths. The percentage increase is defined as the amplitude difference divided by the amplitude without a magnetic field included. The percentage gradually increases from $t = 1.0$ ns as the R-L effect is enhanced due to the increasing field

https://doi.org/10.1017/hpl.2024.3 Published online by Cambridge University Press

strength and the ablation stabilization is weakened. The percentage reaches a peak value of about 20% and the corresponding moment for the short wavelength (i.e., $\lambda = 10$ μm) is earlier than that of the long wavelength cases ($\lambda = 20$ and 30 μm), since the generation rate of the self-generated magnetic field increases as the wavelength decreases due to the larger gradients of density and temperature, which is shown in Figure 9(b), where the rate of magnetic flux generation is defined as $\mathrm{d}\left(\int |B| \mathrm{d}S\right)/\mathrm{d}t$. The generation rates are in agreement with Ref. [42]. As the magnetic field continues to accumulate near the ablation front, the $\kappa_\wedge$ coefficient decreases and the R-L effect is inhibited. The heat flux is less deflected and re-concentrates at the spike tip, resulting in a decrease in the percentage, and the derivative of the amplitude difference $\mathrm{d}(\Delta\eta)/\mathrm{d}t$ also demonstrates this viewpoint. The trend of the averaged $\kappa_\wedge/\kappa_\parallel$ is similar to that of Figures 9(c) and 9(d), peaking at a maximum value and then decreasing (not shown here for brevity).

In order to simplify the simulation model, the radiation is neglected in the simulations. As for the perturbation wavelength of $\lambda = 20$ μm, simulations with considering the radiation are carried out, where the self-generated magnetic field is neglected. The linear growth rate is reduced to $\gamma = 3.04\ \mathrm{ns}^{-1}$, which can be attributed to the smooth density gradient on the ablation front due to the preheating of X-rays and the reduced acceleration due to the radiation energy loss.

4. The importance of the nonlocal effect

The nonlocal thermal transport has the potential to reduce the nonlinear growth of high-mode perturbation with a short wavelength[43]. Currently, the FLASH code does not support a self-consistent coupling between the nonlocal effect and the magnetic field. However, it is still necessary to evaluate the importance of the nonlocal effect. The Knudsen number is an indicator used to quantify the nonlocal effect. It is defined as the ratio of the electron mean free path and the temperature scale length, $\mathrm{Kn} = \lambda_{ei}/L_T$. Figure 10(a) shows the distribution of the temperature gradient scale length $L_T = T_e/|\nabla T_e|$ and the electron mean free path λ_{ei} along the y-axis at $t = 2.0$ ns. It can be seen that L_T is much greater than λ_{ei} by two orders of magnitude. The distribution of Kn along the y-axis is plotted in Figure 10(b), along with the mass density. The Knudsen number around the critical density surface is about $\mathrm{Kn} = 2.66 \times 10^{-3}$ and the peak value is $\mathrm{Kn} = 2.76 \times 10^{-3}$.

In addition to the thermal transport, the Biermann battery effect and the Nernst effect are both dependent on the temperature gradient and would be influenced by the nonlocal effect, called nonlocal suppression. The suppression factor for the Biermann battery effect is $f_B = \frac{1+a_1 d}{1+a_2 d+(a_3 d)^2}$ according to Equation (21) in Ref. [44], where d denotes the nonlocality parameter, similar to the Knudsen number. The Nernst suppression factor is fitted to be $f_N = 0.0566\mathrm{Kn}^{-0.593}$ according to Equation (7) in Ref. [45]. It is mentioned that the fit for f_N is valid in the interval of $\mathrm{Kn} = [0.009, 0.22]$. The Knudsen number near the ablation front in our manuscript has already fallen below the lower limit. As Kn decreases, the f_B and f_N factors both increase until reaching units and the nonlocal suppression is weakening. The suppression factor of f_B is larger than 0.998 near the ablation front, indicating that the nonlocal suppression for the Biermann battery effect and the Nernst effect is reasonably insignificant.

Our previous work points out that the nonlocal effect is dependent on both the laser intensity and the laser frequency, and $\mathrm{Kn} = 7 \times 10^{-3}$ is artificially used as the dividing point between the local and nonlocal effects[46]. The laser intensity threshold for considering the nonlocal effect is $I \sim 1 \times 10^{15}\ \mathrm{W/cm^2}$ for the 3ω frequency. In our paper, a laser intensity of $I = 6 \times 10^{14}\ \mathrm{W/cm^2}$ is employed with the wavelength of $\lambda = 0.35$ μm (correspond to 3ω frequency). As the laser intensity is below the threshold, it can be inferred that the nonlocal effect is of little significance, which is further verified by the simulation results. In the future, we would like to enhance the capabilities of the FLASH code and explore the comprehensive impact of radiation and nonlocal treatment.

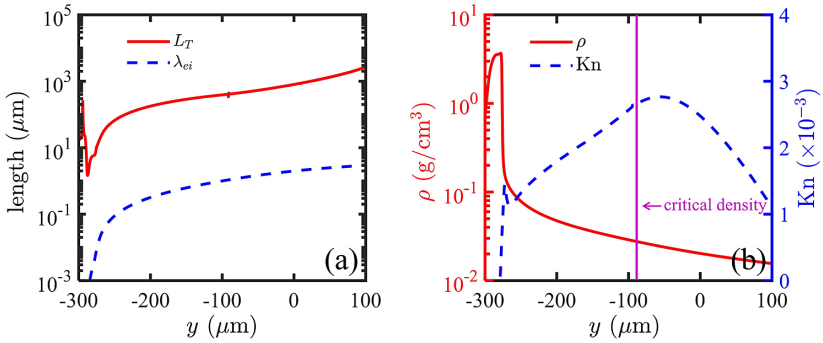

Figure 10. At $t = 2.0$ ns, (a) the distributions of the temperature gradient scale length L_T (red-solid line) and the electron mean free path λ_{ei} (blue-dashed line), (b) the density (red-solid line) and the Knudsen number (blue-dashed line) along the y-axis, which are diagnosed at $x = 0$. The pink-solid line in (b) represents the critical density surface.

https://doi.org/10.1017/hpl.2024.3 Published online by Cambridge University Press

5. Conclusion

To conclude, the self-generated magnetic field and R-L heat flux in the ARTI in a laser irradiating thin target are studied through 2D extended-magnetohydrodynamic simulations. Although the strength of the self-generated magnetic field could reach up to hundreds of teslas during the evolution of the RTI, the plasma is still in a low magnetization state due to cold temperature and high density near the ablation front. The simulations show that the R-L heat flux, additionally generated by the self-generated magnetic field, has a non-ignorable impact during the whole RTI evolution in the acceleration stage. The R-L effect deflects the total heat flux along the spike and towards the spike base. This deflection reduces the heat deposition near the spike tip, lowers the ablative stabilization, allows the spike to penetrate further into the conduction region and results in an increase in the spike-bubble amplitude. The simulations show that the magnetic field increases the linear growth rate by a factor of about 10% compared to the case without a self-generated magnetic field considered. Our results reveal the importance of R-L heat flux and promote deep understanding of the feedback of the self-generated magnetic field on instability evolution, especially during the acceleration stage in ICF.

Acknowledgments

This work was supported by the National Natural Science Foundation of China (Grant Nos. 12175309, 11975308, 12005297 and 12275356) and the Strategic Priority Research Program of the Chinese Academy of Sciences (Grant Nos. XDA25050200 and XDA25010100). Xiao-Hu Yang acknowledges financial support from the Fund for NUDT Young Innovator Awards (Grant No. 20180104) and the Defense Industrial Technology Development Program (Grant No. JCKYS2023212807). Guo-Bo Zhang acknowledges financial support from the Fund for the Research Project of NUDT (Grant No. ZK21–12). The authors are grateful for the useful discussion with De-Hua Zhang of the University of Science and Technology of China.

References

1. D. S. Clark, C. R. Weber, J. L. Milovich, J. D. Salmonson, A. L. Kritcher, S. W. Haan, B. A. Hammel, D. E. Hinkel, O. A. Hurricane, O. S. Jones, M. M. Marinak, P. K. Patel, H. F. Robey, S. M. Sepke, and M. J. Edwards, Phys. Plasmas **23**, 056302 (2016).
2. C. C. Joggerst, A. Almgren, and S. E. Woosley, Astrophys. J. **723**, 353 (2010).
3. K. Lan, Matter Radiat. Extrem. **7**, 055701 (2022).
4. J. D. Lindl, P. Amendt, R. L. Berger, S. G. Glendinning, S. H. Glenzer, S. W. Haan, R. L. Kauffman, O. L. Landen, and L. J. Suter, Phys. Plasmas **11**, 339 (2004).
5. L. F. Wang, H. Y. Guo, J. F. Wu, W. H. Ye, J. Liu, W. Y. Zhang, and X. T. He, Phys. Plasmas **21**, 122710 (2014).
6. L. Wang, W. Ye, X. He, J. Wu, Z. Fan, C. Xue, H. Guo, W. Miao, Y. Yuan, J. Dong, G. Jia, J. Zhang, Y. Li, J. Liu, M. Wang, Y. Ding, and W. Zhang, Sci. China Phys. Mech. Astron. **60**, 055201 (2017).
7. H. Takabe, K. Mima, L. Montierth, and R. L. Morse, Phys. Fluids **28**, 3676 (1985).
8. J. Y. Fu, H. S. Zhang, H. B. Cai, P. L. Yao, and S. P. Zhu, Matter Radiat. Extrem. **8**, 016901 (2023).
9. Y. X. Liu, L. F. Wang, K. G. Zhao, Z. Y. Li, J. F. Wu, W. H. Ye, and Y. J. Li, Phys. Plasmas **29**, 082102 (2022).
10. S. Atzeni and J. Meyer-ter-Vehn, *The Physics of Inertial Fusion* (Oxford Science, Oxford, 2004).
11. K. Lan, X.-T. He, J. Liu, W. Zheng, and D. Lai, Phys. Plasmas **21**, 052704 (2014).
12. O. A. Hurricane, P. K. Patel, R. Betti, D. H. Froula, S. P. Regan, S. A. Slutz, M. R. Gomez, and M. A. Sweeney, Rev. Mod. Phys. **95**, 025005 (2023).
13. I. V. Igumenshchev, A. B. Zylstra, C. K. Li, P. M. Nilson, V. N. Goncharov, and R. D. Petrasso, Phys. Plasmas **21**, 062707 (2014).
14. W. A. Farmer, J. M. Koning, D. J. Strozzi, D. E. Hinkel, L. F. Berzak Hopkins, O. S. Jones, and M. D. Rosen, Phys. Plasmas **24**, 052703 (2017).
15. C. K. Li, F. H. Séguin, J. R. Rygg, J. A. Frenje, M. Manuel, R. D. Petrasso, R. Betti, J. Delettrez, J. P. Knauer, F. Marshall, D. D. Meyerhofer, D. Shvarts, V. A. Smalyuk, C. Stoeckl, O. L. Landen, R. P. J. Town, C. A. Back, and J. D. Kilkenny, Phys. Rev. Lett. **100**, 225001 (2008).
16. M. G. Haines, Can. J. Phys. **64**, 912 (1986).
17. L. Gao, P. M. Nilson, I. V. Igumenshchev, M. G. Haines, D. H. Froula, R. Betti, and D. D. Meyerhofer, Phys. Rev. Lett. **114**, 215003 (2015).
18. C. K. Li, F. H. Séguin, J. A. Frenje, J. R. Rygg, R. D. Petrasso, R. P. J. Town, P. A. Amendt, S. P. Hatchett, O. L. Landen, A. J. Mackinnon, P. K. Patel, V. A. Smalyuk, T. C. Sangster, and J. P. Knauer, Phys. Rev. Lett. **97**, 135003 (2006).
19. K. Mima, T. Tajima, and J. N. Leboeuf, Phys. Rev. Lett. **41**, 1715 (1978).
20. M. J.-E. Manuel, C. K. Li, F. H. Séguin, J. Frenje, D. T. Casey, R. D. Petrasso, S. X. Hu, R. Betti, J. D. Hager, D. D. Meyerhofer, and V. A. Smalyuk, Phys. Rev. Lett. **108**, 255006 (2012).
21. M. J.-E. Manuel, C. K. Li, F. H. Séguin, J. A. Frenje, D. T. Casey, R. D. Petrasso, S. X. Hu, R. Betti, J. Hager, D. D. Meyerhofer, and V. Smalyuk, Phys. Plasmas **19**, 082710 (2012).
22. L. Gao, P. M. Nilson, I. V. Igumenschev, S. X. Hu, J. R. Davies, C. Stoeckl, M. G. Haines, D. H. Froula, R. Betti, and D. D. Meyerhofer, Phys. Rev. Lett. **109**, 115001 (2012).
23. F. García-Rubio, R. Betti, J. Sanz, and H. Aluie, Phys. Plasmas **28**, 012103 (2021).
24. D. Zhang, J. Li, J. Xin, R. Yan, Z. Wan, H. Zhang, and J. Zheng, Phys. Plasmas **29**, 072702 (2022).
25. C. A. Walsh and D. S. Clark, Phys. Rev. E **107**, L013201 (2023).
26. C. A. Walsh, J. P. Chittenden, K. McGlinchey, N. P. L. Niasse, and B. D. Appelbe, Phys. Rev. Lett. **118**, 155001 (2017).
27. D. W. Hill and R. J. Kingham, Phys. Rev. E **98**, 021201 (2018).
28. C. A. Walsh, J. P. Chittenden, D. W. Hill, and C. Ridgers, Phys. Plasmas **27**, 022103 (2020).
29. B. Fryxell, K. Olson, P. Ricker, F. X. Timmes, M. Zingale, D. Q. Lamb, P. MacNeice, R. Rosner, J. W. Truran, and H. Tufo, Astrophys. J. Suppl. Ser. **131**, 273 (2000).
30. D. Lee and A. E. Deane, J. Comput. Phys. **228**, 952 (2009).
31. D. Derigs, A. R. Winters, G. J. Gassner, and S. Walch, J. Comput. Phys. **317**, 223 (2016).
32. S. I. Braginskii, Rev Plasma Phys. **1**, 205 (1965).

https://doi.org/10.1017/hpl.2024.3 Published online by Cambridge University Press

33. J. R. Davies, H. Wen, J.-Y. Ji, and E. D. Held, Phys. Plasmas **28**, 012305 (2021).
34. R. M. More, K. H. Warren, D. A. Young, and G. B. Zimmerman, Phys. Fluids **31**, 3059 (1988).
35. A. Marocchino, S. Atzeni, and A. Schiavi, Phys. Plasmas **17**, 112703 (2010).
36. R. Yan, R. Betti, J. Sanz, H. Aluie, B. Liu, and A. Frank, Phys. Plasmas **23**, 022701 (2016).
37. J.-Y. Ji and E. D. Held, Phys. Plasmas **20**, 042114 (2013).
38. C. A. Walsh, J. D. Sadler, and J. R. Davies, Nucl. Fusion **61**, 116025 (2021).
39. A. Nishiguchi, T. Yabe, M. G. Haines, M. Psimopoulos, and H. Takewaki, Phys. Rev. Lett. **53**, 262 (1984).
40. L. Willingale, A. G. R. Thomas, P. M. Nilson, M. C. Kaluza, S. Bandyopadhyay, A. E. Dangor, R. G. Evans, P. Fernandes, M. G. Haines, C. Kamperidis, R. J. Kingham, S. Minardi, M. Notley, C. P. Ridgers, W. Rozmus, M. Sherlock, M. Tatarakis, M. S. Wei, Z. Najmudin, and K. Krushelnick, Phys. Rev. Lett. **105**, 095001 (2010).
41. R. Betti, V. N. Goncharov, R. L. McCrory, and C. P. Verdon, Phys. Plasmas **5**, 1446 (1998).
42. C. A. Walsh and D. S. Clark, Phys. Plasmas **28**, 092705 (2021).
43. J. Li, R. Yan, B. Zhao, J. Zheng, H. Zhang, and X. Lu, Matter Radiat. Extrem. **7**, 055902 (2022).
44. J. R. Davies, Phys. Plasmas **30**, 072701 (2023).
45. M. Sherlock and J. J. Bissell, Phys. Rev. Lett. **124**, 055001 (2020).
46. Z. H. Chen, X. H. Yang, G. B. Zhang, Y. Y. Ma, H. Xu, S. X. Luan, and J. Zhang, Phys. Plasmas **30**, 062710 (2023).

https://doi.org/10.1017/hpl.2024.3 Published online by Cambridge University Press